Spatial Wavelet Statistics of SAR Backscatter for Characterizing Degraded Forest

Spatial Wavelet Statistics of SAR Backscatter for Characterizing Degraded Forest: A Case Study From Cameroon

Elsa C. De Grandi, *Member, IEEE*, Edward Mitchard, *Member, IEEE*, Iain H. Woodhouse, and Gianfranco D. De Grandi, *Fellow, IEEE*

***Abstract*—Forest degradation is an important issue in global environmental studies, albeit not yet well defined in quantitative terms. The present work addresses the problem, by starting with the assumption that forest spatial structure can provide an indication of the process of forest degradation, this being reflected in the spatial statistics of synthetic aperture radar (SAR) backscatter observations. The capability of characterizing landcover classes, such as intact and degraded forest (DF), is tested by supervised analysis of ENVISAT ASAR and ALOS PALSAR backscatter spatial statistics, provided by wavelet frames. The test is conducted in a closed semideciduous forest in Cameroon, Central Africa. Results showed that wavelet variance scaling signatures, which are measures of the SAR backscatter two-point statistics in the combined space-scale domain, are able to differentiate landcover classes by capturing their spatial distribution. Discrimination between intact and DF was found to be enabled by functional analysis of the wavelet scaling signatures of C-band ENVISAT ASAR data. Analytic parameters, describing the functional form of the scaling signatures when fitted by a third-degree polynomial, resulted in a statistically significant difference between the signatures of intact and DF. The results with ALOS PALSAR, on the other hand, were not significant. The technique sets the stage for promising developments for tracking forest disturbance, especially with the future availability of C-band data provided by ESA Sentinel-1.**

***Index Terms*—Degraded forest (DF), spatial statistics, synthetic aperture radar (SAR), texture, wavelet transform.**

I. Introduction

FORESTS play a fundamental role in the exchange of gases and energy between the atmosphere and biosphere. In particular, degraded forests (DFs) in tropical forest ecosystems are a large component of the global carbon balance, with the process of degradation representing a large but hard to quantify source of carbon, whereas regrowing DFs are also responsible for a significant carbon sink [1]. Recognition of the role of deforestation and forest degradation by the U.N. General Assembly has stressed the need for mapping the extent of deforested and degraded forests [2], in order to enable a successful system for reducing emission from deforestation and forest degradation (REDD+). The International Tropical Timber Organization estimated that there are up to 850 million ha of tropical forest which have already been degraded [3] due to intensive pressures such as logging, slash and burn agriculture, and shifting cultivation outside of protected areas.

Forest degradation in a remote sensing context can be defined from the ecological standpoint and at a conceptual level as an environmental change process, where a disturbance causes the system to evolve from an initial state toward a final state with loss of valuable properties (e.g., canopy cover or carbon stocks) or capacities (e.g., provision of fuelwood and other ecosystem services). This initial state constituted a spatially contiguous and unmanaged old-growth forest [intact forest (IF)]. If some of its structural and physical properties are affected by a major disturbance (logging, fire, insect infestation, timber harvest, or windthrow), then the system will change to a final state, characterized by a different forest type (i.e., secondary forest or disturbed forest).

A mapping between the ecological process of forest degradation and physical observables is needed to provide measures of its onset and extent. The basic tenet of the work presented in this paper is that the process of forest degradation will result in a change of the forest structure. As a consequence, the mapping was established by considering synthetic aperture radar (SAR) backscatter spatial statistics (texture) as a measure of forest structure, this in turn being one of the ecological variables that can be assumed to be a fingerprint of the degradation process. Different stages of the degradation process will result in changes of the statistics. For instance, removal of part of an old-growth forest will correspond to the transition from some stationary regime due to backscattering from the irregular top layer of the canopy [e.g., K-distributed with an exponential cosine autocorrelation function (ACF)] [4] to some nonstationary or intermittent regime. At the final stage of regrowth, when a secondary forest will have taken place, the statistics will revert back to stationary, albeit with different correlation properties due to the different horizontal structure.

This starting assumption is tested by supervised statistical analysis of spatial random fields (SRFs) provided by SAR observations at C- and L-band, i.e., calculating statistics over

Manuscript received September 30, 2014; revised February 14, 2015; accepted March 23, 2015. This work was supported in part by the School of GeoSciences, University of Edinburgh, and in part by the Principal's Career Development Scholarship, University of Edinburgh. The work of E. Mitchard was supported by a Research Fellowship from the Natural Environment Research Council (NE/I021217/1).

E. C. De Grandi, E. Mithcard, and I. H. Woodhouse are with the School of GeoSciences, University of Edinburgh, Edinburgh EH9 3FF, U.K. (e-mail: E-De-Grandi@sms.ed.ac.uk; edward.mitchard@ed.ac.uk; i.h.woodhouse@ed.ac.uk).

G. D. De Grandi was with European Commission, Joint Research Center, Ispra 21027, Italy. He is now with Aberystwyth University, Aberystwyth SY23 3F, U.K. (e-mail: gid6@aber.ac.uk).

Color versions of one or more of the figures in this paper are available online at http://ieeexplore.ieee.org.

Digital Object Identifier 10.1109/JSTARS.2015.2420596

areas of interest based on expert knowledge and the interpretation of other satellite. The spatial statistics are derived from a signal representation in a wavelet frame basis. The analysis seeks to assess the capability of these textural measures to discriminate between intact and DF.

This paper is organized as follows. In Section II, the role of remote sensing for mapping forest degradation is explained. In Section III, the test site of the present work is described. Methods for SAR data processing and analysis are found in Section IV. Results are reported and discussed in Section V. Section VI summarizes the findings and gives concluding remarks.

II. Background and Context

Remote sensing plays a primary role for mapping and monitoring deforestation and forest degradation for REDD+ [5]. In particular, compared to deforestation, forest degradation is more difficult to detect using remote sensing [6], [7].

Mapping and monitoring of forest degradation has been accomplished using optical remote sensing due to the availability of Landsat [8], [9] and the distinct spectral response of DF [10]. Fine resolution optical sensors have been most successfully employed for mapping selective logging, including IKONOS [11] and RapidEye [12]; but to our knowledge, such methods have not been used to map actual forest degradation (as opposed to the presence of logging roads) in African forests.

Limitations of optical sensors have given impetus to the use of sensors independent of atmospheric conditions, such as SAR, which allows observations regardless of cloud cover and illumination conditions, but most importantly is sensitive to both forest vertical structure (through interferometry) and horizontal structure (through backscatter and coherence).

Five main aspects related to forest degradation have been the focus of research: 1) above-ground biomass and carbon stock changes using SAR backscatter (e.g., [13]); 2) classification of DF and particularly the contribution of texture (focus of the present research); 3) detection of the removal of single trees using very high resolution SAR imagery (e.g., [14]); 4) use of interferometric phase information to determine a change in the canopy structure which can be associated with removal of vegetation (e.g., [15]); and 5) use of coherence to provide information on canopy openness [16].

The future provision of Sentinel-1 (C-band) will enable to study forest degradation at increased revisit time leading to unprecedented levels of SAR data availability [17]. However, currently, data coverage is limited due to the recent launch of Sentinel-1.

A further topic of interest is the classification of DF, which can be accomplished with the addition of texture that provides complementary knowledge to intensity-only information [18].

The main research that has been employed in the domain of texture analysis for landcover classification includes the use of Haralick parameters based on gray-level cooccurrence matrix (GLCM) ([19]) and spectral analysis (or ACF, these being techniques in the Fourier transform domain). Notice that the ACF provides a two-point statistics, while GLCM is a second-order one-point one.

The limitations in using these methods for the classification of SAR data are twofold. First, direction constraints on GLCM and insensitivity to short-lived high frequencies in the Fourier transform limit the ability of these methods to quantify the evolution of statistical properties through scale [20]. Second, by their nature, SAR sensors are affected by both multiplicative noise and correlated noise: this means that simple relationships among neighboring pixels can either bear no information, being themselves just stationary white noise, or even provide false information; for instance, two constant reflectivity areas might be measured as two textured areas because of the presence of speckle. GLCM and ACFs are both highly sensitive to speckle noise. A way out suggested in related work such as in [21] is to apply these statistics after transforming the input signal to the logarithmic domain. This transform makes the multiplicative noise additive. However, introduces side effects such as compressing high dynamics features and boosting low-level noise, such as thermal noise.

Wavelet transforms provide a modern pathway to time-frequency (space-scale) analysis with better resolution in the combined domain, and superior computational efficiency on the discrete setting. Moreover, wavelet statistics can be normalized in such a way as to be compatible with multiplicative noise without recurring to the logarithmic transform (see Section IV-C)

The field of wavelets developed in the mid-1980s with research by [22]. Originally, wavelet transform developed in the field of geophysics applied to time-series analysis of one-dimensional (1-D) geophysical signals [23]; but since then have been applied in the field of remote sensing including landcover classification using SAR, which is becoming more popular [24].

Techniques based on the use of wavelet transform with SAR imagery have seldom been used in the thematic context of forest degradation. However, wavelet statistics of SAR backscatter in connection with textural analysis was proposed in a different thematic context in [25]and [26] and in general, its utility in image processing have been long understood [27].

III. Study Site

We center our study in Cameroon, a country of great interest for forest monitoring, since it is the African country with the highest percentage of previously logged forests [28]. Over a third of its territory is covered by moist tropical forest, part of the Congo Basin, and the area covered by active or previously active logging concessions extends over $71\,000\,\mathrm{km}^2$, about 40% of total forest area [29]. Cameroon is also a significant hotspot of other forms of forest degradation, including those related to agricultural encroachment, fuelwood extraction, and illegal logging [28]: it is more affected by these than its Congo basis neighbors as it has a significantly higher population density than neighboring Gabon, Democratic Republic of the Congo, or the Republic of Congo.

The study site encompasses semideciduous closed forest located in Deng Deng National Park and its surroundings in Lom et Djerem, Cameroon (13°4′ E, 5°28′39 N). The study site extends for 100×100 km and is delimited by the Sanaga River to the west and the forest savanna transition zone to the

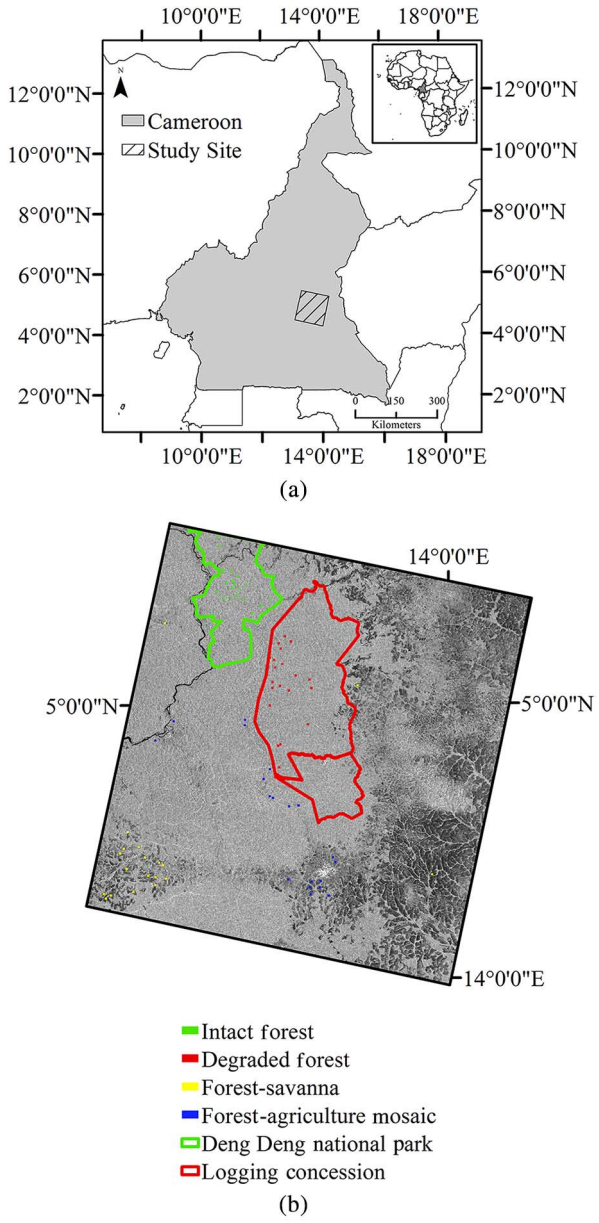

Fig. 1. (a) Study area within the extent of ENVISAR ASAR acquisitions (WGS84, UTM zone 33 N). (b) Location of all landcover samples (n = 20) used in the analysis overlaid on ENVISAT ASAR VV (WGS84, UTM projection-zone 33N). Data source: World Resources Institute and European Space Agency. The green shape outlines the Deng Deng National Park. The yellow shape outlines a logging concession. Red squares mark samples of DF within the concession, green squares mark IF samples in the National Park, yellow squares mark samples within FS and blue squares mark samples within FAM (see also Table II).

east (Fig. 1). The main urban center in the area of study is the region's capital Bertoua while, a high number of rural villages are distributed across the landscape contributing to the highest rate of rural population exploiting forest resources mainly in the form of slash and burn agriculture at small to medium scales [30]. The forest in the area is a semideciduous closed forest dominated by *Sterculiaceae* and *Ulmaceae* and extends to the north of the moist evergreen forest [31]. Human intervention is widespread in the area giving rise to several stages of DF and areas of regenerating forest developing into secondary formations characterized by *Musanga cecropioides* and *Albizia spp*. [32].

Another driver of forest degradation is selective logging within the forest management units (UFAs). The logging industry has been present in the area and exploited forest resources through the selective removal of a limited number of high-value trees. Even though the UFA had been exploited long in the past, the presence of old logging roads was still clearly visible in the 2010 Landsat and RapidEye imagery (and less evident in radar imagery).

The climate is classified as equatorial (Guinean type) with one major wet season (September–November) (monthly rainfall over 250 mm) and dry season with rainfall as low as 10 mm (December–February) [33]. Rainfall at the time of ENVISAT ASAR data acquisition (January 15, 2010) and ALOS PALSAR (August 3, 2010) can be considered negligible, since the data was acquired in the dry season. Topography in the study site is hilly to mountainous ranging from 597 to 1060 m with areas of more pronounced topography located to the north of the study site in the forest-savanna (FS) mosaic, whereas topography is more gentle in the areas of semideciduous forest (ranging between 597 and 700 m a.s.l.).

IV. Methods

Methods employed for the analysis of both ENVISAT ASAR (VV) and ALOS PALSAR (HH and HV) scenes comprise the following steps: 1) SAR data processing; 2) thematic class definition and supervised selection of a spatial test set for SAR statistics estimation (43×43 pixels windows) for each class; and 3) wavelet transform of the test set SRFs and wavelet coefficients statistics computation and interpretation.

A. SAR Data Processing

Nine ENVISAT ASAR IMS scenes were acquired between 2003 and 2010 at VV polarization, IS2 mode (23° incidence angle) over the study area. The datasets were processed using the basic processing module available with SARscape 5.0 software [34]. The scenes were multilooked, coregistered, radiometrically calibrated and radiometrically normalized (cosine correction) using a 90-m SRTM DEM, geocoded to WGS84, UTM projection (zone 33N) at 15-m pixel spacing. Importantly, the time-series was speckle filtered using "De Grandi multitemporal filter" available in SARscape 5.0 and based on the principles proposed in [35]. This step enables the reconstruction of the radar cross-section (RCS) with good preservation of its two-point spatial statistics, whereas abating the strength of the high-frequency noise induced by the fading process to a level inversely proportional to the number of samples in the series. It is therefore fundamental with respect to the capability of retrieving textural properties of the imaged target.

Most of the analysis presented here was then undertaken on a single ENVISAT ASAR scene (January 15, 2010), since it was acquired during the dry season with minimal influence from rainfall events and, correspondent with available ALOS PALSAR and RapidEye data.

Twelve ALOS PALSAR fine beam dual (FBD) were acquired between 2007 and 2010 at HH and HV polarizations and 34° incidence angle. This dataset was processed using the same approach as above.

Supplementary optical data for the interpretation of SAR imagery consisted of Landsat ETM+ (slc-off) at 30-m resolution acquired on January 18, 2011 covering the northernmost part of the study site and Landsat ETM+ (slc-on) data acquired on December 27, 2002 covering the southern part of the study area. The scenes were the only available which were not affected by extensive cloud cover and closest to the data of the SAR data acquisition. RapidEye at 5-m resolution was also acquired on December 17, 2010 for training purposes covering a selected area of UFA 10 065 and part of Deng Deng National Park. Contextual data consisting of UFAs, logging roads (digitized with the aid of Landsat), location of protected areas (e.g., Deng Deng National Park) were provided by [36]. The data were used to help with the selection of classes of interest through a supervised analysis.

B. Spatial Test Set Preparation by Supervised Analysis

A supervised analysis was chosen due to unavailability of ground truth data for 2010, thus the use of optical imagery and contextual information was used for training purposes. The analysis uses a 43×43 pixel window (corresponding to 645×645 m on ENVISAT ASAR and ALOS PALSAR geocoded scenes at 15 m pixel spacing). The classes selected correspond to the following: IF, DF, forest-agriculture mosaic (FAM), and FS. Four samples were used in parts of the analysis but twenty samples were selected for each class of interest to ensure a significant sample size for statistical analysis.

IF areas were selected based on contextual information including the extent of Deng Deng National Park and the absence of logging roads and urban centers in the areas chosen. The chosen areas are all located in the northern section of the Deng Deng National Park, which is known to be intact and has no sign of logging roads in any ancillary dataset.

DF was identified based on the presence of inactive logging roads (in 2010) which were clearly visible in both Landsat and RapidEye data at the time of the analysis and were also noticeable back in the 1980s Landsat imagery, thus indicating the long term pattern of disturbance of forest inside the logging concession. FAM could be clearly identified in both Landsat and RapidEye scenes as the most complex and heterogeneous class among those selected due to the presence of a mixture of forest, bare areas, and agricultural fields. The pattern of anthropogenic disturbance was also very clear due to the proximity to rural settlements. FS presented lower backscatter values in ENVISAT ASAR VV and ALOS PALSAR HH and HV scenes compared to dense forested areas.

C. Spatial Statistics From a Wavelet Frame Basis Representation

The spatial statistics of interest are derived from a signal (field) representation provided by a nonorthogonal oversampled discrete wavelet transform (DWT). The basis for this representation is generated by a wavelet frame [37]. The advantage of such an approach in connection with texture (spatial statistic) analysis is proven in [27]. In our case, the mother wavelet in the continuous scale-space domain is the first derivative of a box spline of order 3 [38] (see Fig. 2), with Fourier transform

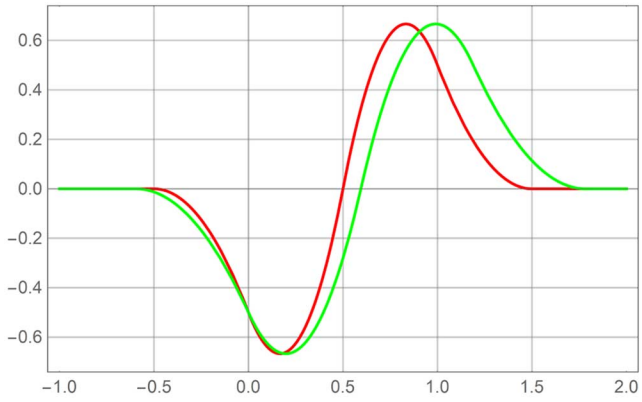

Fig. 2. Mother wavelet (red line) and the dilated by $2^{0.25}$ version (first and second voice).

$$\hat{w}(\omega) = -i\frac{\omega}{4}\left(\frac{\sin\left(\frac{\omega}{4}\right)}{\frac{\omega}{4}}\right)^4 e^{-i\frac{\omega}{2}}. \tag{1}$$

In the discrete case, the transform is implemented using a variant of the à trous algorithm [39], [40] with four voices per octave. The design of the multivoice scheme entails the following steps. For each voice in the first octave, a fractionally dilated wavelet is computed in the frequency domain from (1)

$$\Psi_{\mathrm{dil}}(\omega) = \frac{1}{\sqrt{2^d}} 2^d \Psi\left(2^d\omega\right) e^{-i\omega\left(\frac{1}{2}(2^d-1)\right)} \tag{2}$$

where the fractional dilation factor is $d = 0.25\,k, k = 0 \cdots 3$. The dilated wavelet is normalized by $\frac{1}{\sqrt{2^d}}$ to preserve the norms, and shifted by $e^{-i\omega\left(\frac{1}{2}(2^d-1)\right)}$ in such a way so as to match the zero crossings of the original mother wavelet.

Importantly, the multivoice scheme using the à trous algorithm can only be implemented with the $s^{-1/2}$ normalization to assure equal norms among the mother wavelets which sample the frequency lattice within one octave. In this way, wavelet coefficients corresponding to all voices and octaves carry comparable energy, and can be used in forming measures, e.g., two-point statistics of the signal.

The à trous algorithm [39], [40] calls for the approximation of the continuous space wavelet by means of an interpolating filter. This condition is expressed in the time and frequency domain by

$$\frac{1}{\sqrt{2}}\psi\left(\frac{t}{2}\right) = \sum\nolimits_n h[n]\,\phi(t-n) \tag{3}$$

$$\frac{2}{\sqrt{2}}\Psi_{\mathrm{dil}}(2\omega) = H_j(\omega)\,\Phi(\omega). \tag{4}$$

The high-pass filter coefficients for each fractionally dilated wavelet are computed from (4) by inverse discrete Fourier transform (DFT)

$$h_j[n] = \frac{1}{2\pi}\int_{-\pi}^{+\pi} H_j(\omega)\, e^{i\omega n} d\omega \tag{5}$$

where j is the voice index.

Each dilated high-pass filter h_j for each voice is finally used in a recursive à trous decomposition scheme to generate wavelet coefficients at the corresponding dyadic scales $2^{d+j}, j = 1 \ldots n$.

In case of analysis of a two-dimensional (2-D) field, the DWT is implemented by separable (row, columns) convolutions with a low-pass and a high-pass filter [40]

$$\begin{aligned} f_{s+1}(i,j) &= g_s(j)\, g_s(i) \otimes_j \otimes_i f_s(i,j) \\ c_{x,s+1}(i,j,v) &= h_s(j,v) \otimes_j f_s(i,j) \\ c_{y,s+1}(i,j,v) &= h_s(i,v) \otimes_i f_s(i,j) \end{aligned} \tag{6}$$

where $\bigotimes_j$ is the convolution operator over columns, and $\bigotimes_i$ is the convolution operator over lines, $f_1(i,j)$ is the input signal, h_s is high-pass filter at level s and voice v, g_s is low-pass filter (à trous filter) at level s, both filters being upsampled by dilation with s zeros.

In a nutshell, the multivoice scheme for v voices is implemented by applying the à trous algorithm, valid for power of two scales, v times starting from each fractionally dilated mother wavelet.

Importantly, the wavelet coefficients in (6) are normalized by smooth approximations of the input fields $\overline{\overline{f(i,j)}}_s$ at the corresponding scale s. The smooth approximations are obtained by convolution with separable smoothing spline filters with unit norm (energy conserving) and dilated by a factor corresponding to the scale s. This position (as pointed out in [25]) is necessary to avoid influence on the wavelet statistics of the fading variable when multiplicative noise is developed, and to equalize the dynamic range of the variable of interest (RCS). Theoretical characterization (bias and variance) of estimators of normalized wavelet coefficients is given in [41].

The mother wavelet (Fig. 2) acts as a differential operator. It is this characteristic that establishes the bridge for reaching over to the spatial statistics of interest. Indeed, a wavelet which is a symmetric and odd function of the space coordinate (as the one considered here), when translated performs differences between averages of the signals around points whose distance is proportional to the dilation factor (scale). This leads to consider the following equivalence between local averages of the wavelet coefficients squared and a two-point statistic known as structure function of order 2

$$\langle {c_{x,s}}^2 \rangle \cong \langle (f(x+\tau) - f(x)^2 \rangle, \quad \text{where } s \overset{yields}{\longrightarrow} \tau \tag{7}$$

where $\langle\rangle$ is a spatial average operator.

In turn, this statistic leads to the characterization of stationary random processes, as well as of nonstationary processes with stationary increments (e.g., fractals) [42]). The wavelet variance as a function of scale provides in the log–log variance/scale plane a characteristic signature of the process and measures of the process parameters, such as correlation structures in stationary processes and the scaling exponent in 1/f processes.

Computationally, the wavelet scaling signature (WASS) is estimated from the wavelet coefficients of the 2-D DWT (6) within a 43×43 pixels window of the backscatter image centered around points of interest (see Section IV-B for the selection criteria)

$$\begin{aligned} WS_x(s) &= \langle c_{x,s}(i,j)^2 \rangle \\ WS_y(s) &= \langle c_{y,s}(i,j)^2 \rangle \end{aligned} \tag{8}$$

where the average is taken over the estimation window. The standard error of the wavelet variance estimator S^2 (8) is $\sigma_{S^2} = S^2\sqrt{\frac{2}{n-1}}$, where n is the number of samples in the estimation window.

When a second realization of the input random field is available, this being acquired at a different date or with different sensor's configuration (e.g., polarization, incidence angle), a scaling signature can be constructed with the wavelet coefficients cross-correlation

$$\begin{aligned} WCRS_x(s) &= \frac{\langle c_{x,s^1}(i,j)\, c_{x,s^2}(i,j) \rangle}{\left(\langle c_{x,s^1}(i,j)^2 \rangle \langle c_{x,s^2}(i,j)^2 \rangle \right)^{1/2}} \\ WCRS_y(s) &= \frac{\langle c_{y^1}(s,i,j)\, c_{y^2}(s,i,j) \rangle}{\left(\langle c_{y,s^1}(i,j)^2 \rangle \langle c_{y,s^2}(i,j)^2 \rangle \right)^{1/2}}. \end{aligned} \tag{9}$$

In the case of spatial statistics, this signature provides an indicator of the textural difference of the observed random fields between acquisitions. For acquisitions at different dates, the wavelet cross-correlation extends the statistics to the time–space–frequency domain.

A second point of view leads us to consider the generation of a scale-dependent gradient field $\epsilon(s,x,y)$ from the wavelet coefficients, which in turn can be used as a random measure in intermittency analysis. Intermittency in our context can be generated in a random field by the presence of singularities such as edges and point targets. The normalized fourth moment of the gradient modulus (called the flatness factor) is taken in this case as an indicator of intermittency within the random field. Indeed, the fourth moment of a probability density function (pdf) (kurtosis) is related to the flatness of the distribution's tails. Since the wavelet frame is a differential operator, thick tails of the distribution indicate the presence of spikes or events with high derivative. The wavelet flatness factor signature (dependence on scale) is computed in a way similar to the wavelet scaling signature (9)

$$\begin{aligned} FlS_x(s) &= \frac{\langle c_{x,s}(i,j)^4 \rangle}{\langle c_{x,s}(i,j)^2 \rangle^2} \\ FlS_y(s) &= \frac{\langle c_{y,s}(s,i,j)^4 \rangle}{\langle c_{y,s}(s,i,j)^2 \rangle^2}. \end{aligned} \tag{10}$$

Finally, the gradient field modulus squared can be interpreted as the signal energy captured at every point visited by the translated and dilated wavelet in the space-scale lattice and within the resolution cell at that point (Heisenberg box [38]). Local estimates of the $\epsilon(s,x,y)$ field through the related wavelet coefficients provide a space–frequency analysis of the input random field energy, which is called the wavelet spectrum. The wavelet spectrum is computed by convolution of the wavelet

TABLE I
WAVELET RESOLUTION FOR THE FIRST FOUR VOICES

Scale	σ_{space}(m)	σ_{period}(m)	σ_{freq} (cycles /winl)
2^0	11.34	4.20	1513
$2^{0.25}$	13.48	5.19	1227
$2^{0.5}$	16.03	9.42	675
$2^{0.75}$	19.07	19.76	322
2	22.68	40.61	156

coefficients with a smoothing kernel (a cubic spline β_m, with support $\mathrm{m} = 25$ pixels)

$$Wspctr\,(s,i,j) = \left(c_{x,s}(i,j)^2 + \langle c_{y,s}(i,j)^2\rangle\right) \otimes \beta_m\,(i,j)\,. \tag{11}$$

Since $Wspctr\,(s,i,j)$ is a function of three variables, a three-dimensional (3-D) graphic representation is obtained by averaging in one direction (columns or rows). The spectrum is then pictured in a 2-D density plot, with space, scale on the x-, y-axis and a color palette to represent power density.

In space-scale (time–frequency) analysis, which underpins all the derived spatial statistics considered here, the most important factor is the combined resolution in the two dimensions of the domain. Wavelet provides adaptive resolution with increased frequency support and short-time spread at short scales, and decreased frequency support and wider time spread at long scales. It is important to quantify the combined resolutions and to put these measures in comparison with the order of magnitude of space variations expected in the physical phenomenon of interest (e.g., forest canopy horizontal distribution). The space and frequency spread of the wavelet was computed as follows.

The wavelet $\psi\,(s,x)$ at each scale s is normalized in such a way that $\|\psi\| = 1$ and shifted to be centered at $\mathrm{x} = 0$. In this way, the spread in space and frequency is

$$\sigma_x^2 = \int_{-\infty}^{+\infty} x^2\psi^2 dt \tag{12}$$

$$\sigma_\omega^2 = \int_{-\infty}^{+\infty} (\omega-\eta)^2\hat{\psi}^2 d\omega \tag{13}$$

where $\hat{\psi}$ is the Fourier transform of ψ and η is the center frequency.

The spread σ_x and σ_ω were computed for the first four voices (Table I).

In Table I, $\sigma_{space}\,(m)$ is the resolution in space related to the reference system of the geocoded SAR imagery with a pixel spacing of 15 m. $\sigma_{period}\,(m)$ is the resolution if frequency given as a period $T = \frac{2\pi}{\omega}$, where ω is the frequency in radians/m. $\sigma_{freq}\,(\mathrm{cycles/winl})$ is the resolution in frequency given as number of cycles within the estimation window length.

Values in the table can be interpreted as follows. First, notice that resolutions in the space-scale (time–frequency) plane were computed for the continuous wavelet transform, therefore, space is defined on the real numbers set, and the support of the mother wavelet at scale 1 is in $d = [-1, 1]$. Normalized values in the space domain are then converted in metric units with $d \triangle x\,[\mathrm{m}] = [-15, 15]$. Values at the next dyadic scales can be computed simply by multiplication (division) by 2.

With these figures in mind, let us imagine of considering a backscatter signal portraying intermittent hard targets (e.g., buildings) and periodic features (e.g., a forest canopy or ocean waves). Values $\sigma_{space}\,(\mathrm{m})$ tell us that we could distinguish, by the wavelet multiscale representation, the impulsive features if they are spaced apart a distance greater than these values. Values $\sigma_{period}\,(\mathrm{m})$ tell us that we could detect the periodic features if their period is greater than those values. Finally, the last column gives us an indication of how many oscillations of the periodic phenomena we could at most observe within an estimation window of 615 m.

In our thematic context, we could for instance conclude regarding space resolution: The first four voices do not provide useful information, being the resolution less than the sensor's one; intermittency patterns with characteristic spacing of $2^j \times 23\,\mathrm{m}$ will be best detected at corresponding resonating scales 2^j. Regarding frequency resolution, the spatial frequency components of an homogeneous forest canopy, this developing with a characteristic period of some $2^j \times 40\,\mathrm{m}$ could be best measured at resonating scales 2^j.

D. Connection Between Wavelet Variance Analysis and Fourier Spectral Analysis

Relevance of two-point statistics in connection with SAR imagery textural characterization, in particular of the Fourier spectral analysis and the ACF, was pointed out in a seminal work published in the late 1980s [43]. This work was targeted to supervised classification, where textural class parameters were estimated from SAR spatial statistics. Analysis was carried out based on stationary Rayleigh statistics for the envelope of the received field, and under the condition of a delta correlated fading component. In this framework, a method was derived for the estimation of the underlying RCS ACF from experimental data, whereas no specific model for the surface fluctuations was proposed. This line of research was extended by a theoretical model for non-Rayleigh SAR scattering statistics, covering the case of correlations between scatterers in the resolution cell (or fluctuating cross-section), and finite illumination window [44], [45]. The surface fluctuations were described by a Gamma distribution and a Lorentzian spectrum (exponential ACF). This model is particularly relevant when imaging forest at the resolution afforded by instruments used in our experiments. These contributions were the springboard over which interest in space–frequency analysis of SAR backscatter took momentum [46]–[49].

Wavelet frame spatial statistical measures are rooted in the groundwork established by the classical Fourier ACF analysis adopted in those research works, but extend it in several respects: 1) by enabling space-scale analysis (through good localization in the space–frequency domain); 2) by the capability of dealing with nonstationary processes; and 3) providing statistically better and computationally more efficient estimators. The reader is referred to [50] for a discussion on this topic. It appears therefore interesting to establish, for those random processes described by the models mentioned above, the

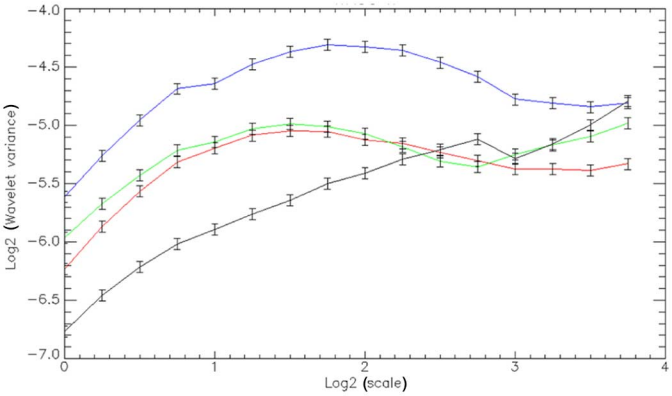

Fig. 3. Wavelet variance scaling signatures computed on single date ENVISAT ASAR VV backscatter (2010) for four classes of interest: FAM (blue), DF (red), IF (green), and FS (black). The error bars correspond to the standard error of the wavelet variance estimator.

TABLE II
FOUR LANDCOVER SAMPLES USED IN THE ANALYSIS (WGS84, UTM PROJECTION—ZONE 33 N)

Class	Center pixel coordinates
IF	329 220 E, 586 850 N
DF	344 085 E, 556 755 N
FAM	306 510 E, 543 045 N
FS	363 405 E, 558 060 N

connection between the wavelet space-scale statistics (wavelet variance and covariance) and the ACF based characterization.

For the purpose, analytical and numerical derivations were undertaken to illustrate the response of the wavelet scaling signatures to given correlation properties of the input SRF, including those assumed in the models in [44]. The gist of the analysis was based on the theory of linear filtering of random signals [51], which was exploited to link the spectral properties of the input signal to the statistics (variance) of the output process, this being filtered by the wavelet operator. Detailed analytical derivations and results would be outside the scope of the paper.

Suffice here to mention that for fractal RCS [52]–[54], the dependence of the wavelet variance on scale is linear in log–log scale, with the first derivative proportional to the spectral exponent. For a Gamma-distributed RCS with exponential ACF [44], the wavelet variance increases nonlinearly with the derivative at scale $\mathrm{s} = 1$ linear in β (the inverse correlation length). While, the asymptotic value is proportional to the second moment of intensity.

V. ENVISAT ASAR RESULTS AND INTERPRETATION

A. Wavelet Variance Signatures

The graph in Fig. 3 shows the wavelet variance as a function of scale (four dyadic scales and four voices) for four classes of interest with corresponding estimation windows selected on ENVISAR ASAR VV backscatter geocoded data (Table II). Notice that in this set of classes and with respect to SAR backscatter, there are two radiometrically pure cases (intact and DF) and two mixed cases (FAM and FS). However, in terms of textural analysis, these classes can be handled as pure classes, in the sense that they can be characterized by separable measures.

The following observations can be made. Regarding the general trend with scale, signatures related to IF, DF, and FAM all show the fingerprint of a stationary random process with loss of correlation at short scales, a first maximum (sill) in a range of intermediate scales (corresponding to the correlation length concept in Fourier analysis), and a final segment with flattening out (white noise DF, FAM) or the presence of further correlation (or anticorrelation) structures (IF). A striking difference is provided by the FS signature which presents persistent increase with scale, a sign of a nonstationary process. This situation is due to the presence of strong radiometric nonhomogeneities within the estimation area (mixture), due to the intertwining of grassland and taller vegetation, as it will be documented later by wavelet spectra analysis (see Section V-D).

Regarding the separation between signatures (in terms of point-wise distance between variance values at each scale with respect to the estimation error), it is clear that between scales 2^0 and 2^2, the two radiometrically mixed classes (FAM and FS) are well separated between themselves and with respect to the union of more homogeneous classes (IF and DF). However, separation between IF and DF appears problematic, when based only on scale-by-scale differences between signature values. Statistical analysis on the probability distribution of the signatures' values for 20 samples of each class confirms these results.

The key to the solution of the problem stems from considering the functional dependence on scale of the signatures, as opposed to their point by point differences. For this purpose, the difference between IF and DF signatures were analyzed in more detail. The two functions (IF and DF signatures) appear to have a very similar form in the range of scales 2^0–2^2. However, the sill (first maximum) of the IF occurs at shorter scale than the DF one, or, in other words, there is a remarkable and consistent difference in the correlation length for the two classes [Fig. 4(a)]. Additionally, the IF signature shows persistent correlation/anticorrelation structures at longer scales, whereas the DF tends to flatten out.

A link between these two statistical correlation patterns and the underlying structure of the observed target can be conjectured in the following way. The IF structure is made up by layers of vegetation and in particular large emergent trees contribute to the signal. Instead, the DF has a relatively more homogeneous structure due to the removal of large emergent trees and the vegetation regrowth which has achieved a stage similar to the remnant vegetation from the intact stage. Let us remember that C-band radiation has a short penetration depth into a dense target, like this type of forest. Therefore, the RCS is spatially modulated by height changes and shadowing effects of a thin layer at top of canopy. Therefore, the IF return (which is more "rough") will decorrelate at shorter scales than the more homogeneous DF. On the other hand, the IF will retain some self-similar structures at longer scales, which will result in long scale memory as far as correlation is concerned. The results concerning the IF are in line with the dense homogeneous forest model in [51], where K-distributed clutter with an exponential cosine ACF is assumed. These considerations suggested a

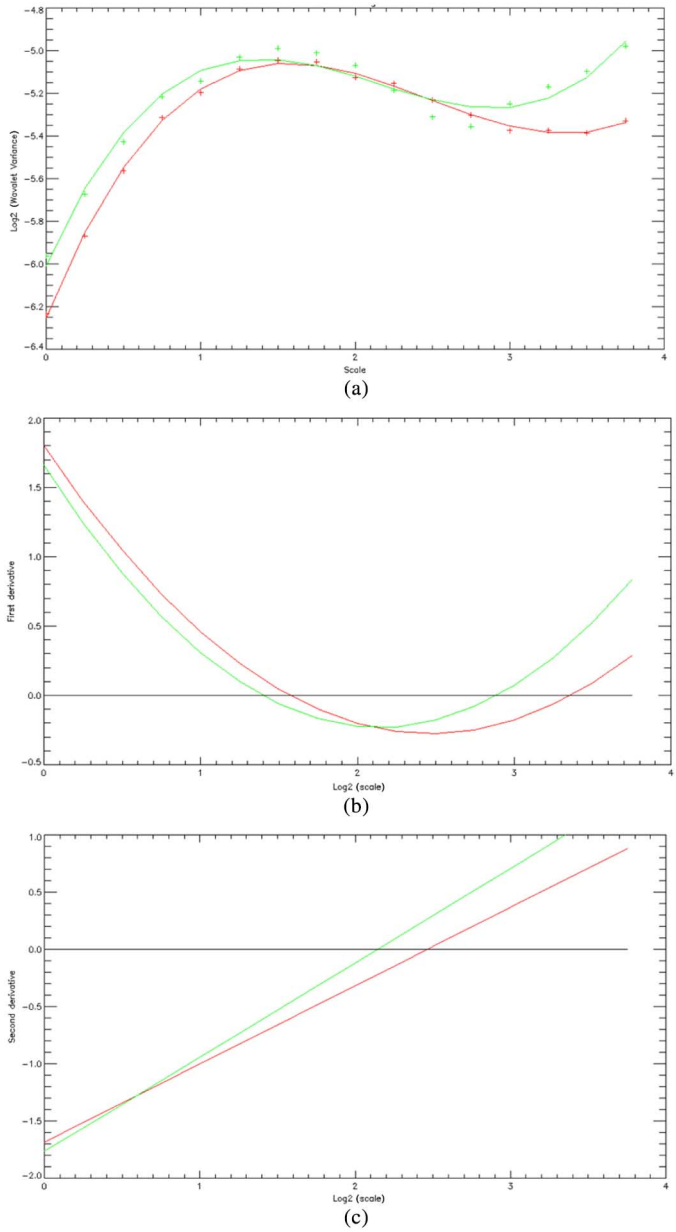

Fig. 4. (a) Wavelet scaling signature for two classes: IF (green cross), DF (red cross), and the fitted third-degree polynomial function (green and red solid lines for IF and DF, respectively). (b) First derivative of the IF (green) and DF (red) fitted wavelet scaling signatures. (c) Second derivative (slope) of the IF (green) and DF (red) fitted wavelet scaling signatures.

computational approach for the two-class pattern recognition problem based on signature functional analysis (described in Section V- B).

B. Wavelet Scaling Signatures Functional Analysis

Functional analysis of the wavelet scaling signatures was undertaken by fitting a polynomial function to the wavelet variance values for two classes of interest: IF (green) and DF (red) [Fig. 4(a)]. The wavelet scaling signatures points were fitted using a third-degree polynomial function of the form $y = ax^3 + by^2 + cx + d$. Two patterns can be noted in the graph: the first maximum (sill) of the IF signature occurs at shorter scale than the DF one; the presence of persistent correlations (anticorrelations) at long scales in the IF signature, whereas the DF signature tends to level off (uncorrelated noise). These two different functional dependences of the wavelet variance on scale can be described by the first and second derivatives of the fitting polynomial, as shown in Fig. 4(b) and (c). The zero crossing of the first derivative marks the onset of the sill point. The zero crossing of the second derivative marks the inflection point of the signature, this occurring always at longer scales for the DF class.

The combination of these functional parameters provides a consistent condition to discriminate between the two classes. This proposition was proven by a statistical hypothesis test of the difference of the parameters' mean values using 20 samples for each class of interest (H0: $\overline{x}_{DEG} - \overline{x}_{IF} = 0$). Concerning the first derivative zero crossings, the test resulted in one-sided p-value equal to 6.477×10^{-7}; thus, H0 was rejected indicating that there is a significant difference between the means at a 0.05 significance level. As to the zero crossings of the second derivative, the test gave a one-sided p-value equal to 0.003 with H0 rejected.

TABLE III
FLATNESS FACTOR STATISTICS FOR 20 SAMPLES OF EACH OF THE FOUR CLASSES OF INTEREST

Scale	DF		IF		FAM		FS	
	Mean	Stdev	Mean	Stdev	Mean	Stdev	Mean	Stdev
2^0	6.01	4.58	3.54	0.18	6.20	7.94	5.84	3.29
2^1	4.28	2.29	3.24	0.24	4.21	2.15	5.90	2.55
2^2	3.58	0.86	3.31	0.28	3.77	0.79	6.7	5.26
2^3	3.58	0.44	3.31	0.35	3.54	0.67	5.49	3.69
2^4	4.12	1.41	3.74	0.46	3.56	0.82	4.57	2.85

DF, degraded forest; IF, infact forest; FAM, forest agriculture mosaic; FS, forest-savanna.

C. Flatness Factor

The flatness factor [see (10)] intuitively gives an indication of the relative variability of the wavelet variance within the data samples, and therefore can indicate the presence of intermittency in the SAR signal, such as edges and point targets. As a guideline for the interpretation of the experimental data, we remind that for a wavelet frame that acts as a differentiator, and for Gaussian white noise as input, the flatness factor equals 3.

IF is the class which presents the lowest amount of intermittency at all scales, and less spread among samples, with flatness factor values around 3, thus pointing at a nearly Gaussian noise process (Table III).

The DF reveals some intermittency at short scales, also with large spread among samples (Table III). This result seems to contrast the conclusion derived from the scaling signature, which indicates the DF as a more homogeneous process than the IF. However, closer examination of the DF areas reveals that these high intermittency values are due to topographic effects (shadow, layover) which are present in some of the areas.

The FAM and FS classes both present intermittency of different importance, with the highest values and highest spread among samples for the FS (Table III). In both these cases, the intermittency is due to the presence of edges between two

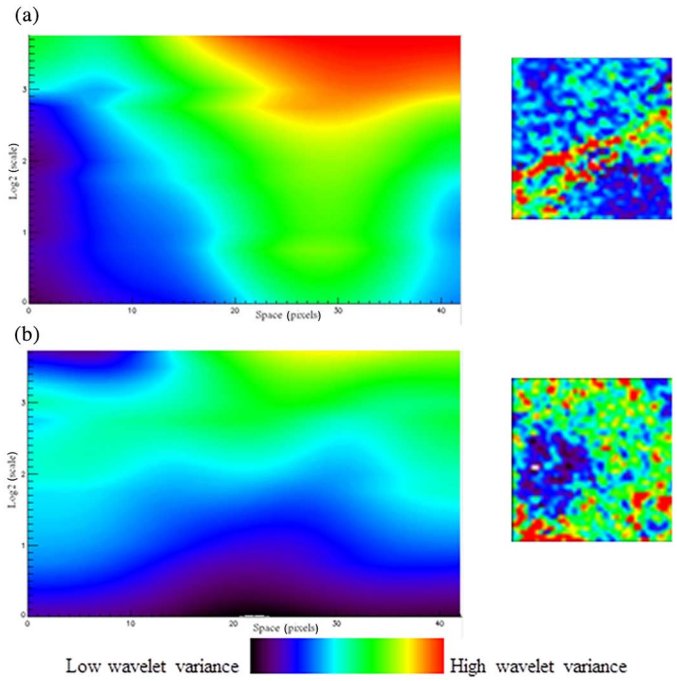

Fig. 5. Wavelet spectrum for (a) FS (in the northing direction) and (b) FAM (easting direction) showing the different textural properties of each class in the space-scale domain. The spectrum is estimated in a 43×43 pixels window (equivalent to 645×645 m in the ASAR geocoded dataset). The SAR backscatter within the corresponding windows (rendered in false color) is shown at the right of the spectra. These test cases highlight the capability of the wavelet space-scale representation to characterize radiometrically heterogeneous targets, such as a forest ribbon in (a) and the margin between bare soil and forest in (b).

homogeneous fields (e.g., soil and forest in FAM, and forest clusters in the FS). These singularities are of different strength, as a function of the related backscatter values, as indicated by higher flatness values with the FS class. The case of these nonstationary samples will be further analyzed using the wavelet spectrum in Section V-D.

D. Wavelet Space-Scale Signatures (Spectrum)

Analysis by wavelet spectrum of the two heterogeneous classes FS and FAM illustrates well the ability of this technique for localizing features in the combined space–frequency domain. The FS spectrum is shown in Fig. 5(a), this being represented in the northing direction. The backscatter in the estimation window (43×43 pixels) for FS and FAM is shown in false color in Fig. 5. A singularity (ridge) due to a forest ribbon is present in the image [Fig. 5(a)]. This feature is mapped onto the triangular area of higher variance values spreading in scale and around pixel 30 in space. Changes of the wavelet variance trajectory with scale are due to the intersection of the translated wavelet with the feature.

The FAM case [Fig. 5(b)] concerns an area with a diagonal edge marking the transition from bare soil to forest. In the spectrum (represented in the easting direction), the first segment (pixels 0–10) reveals a stationary signature (maximum at scale 2) that is due to the bare soil homogeneous region within this range, whereas the following spectrum values

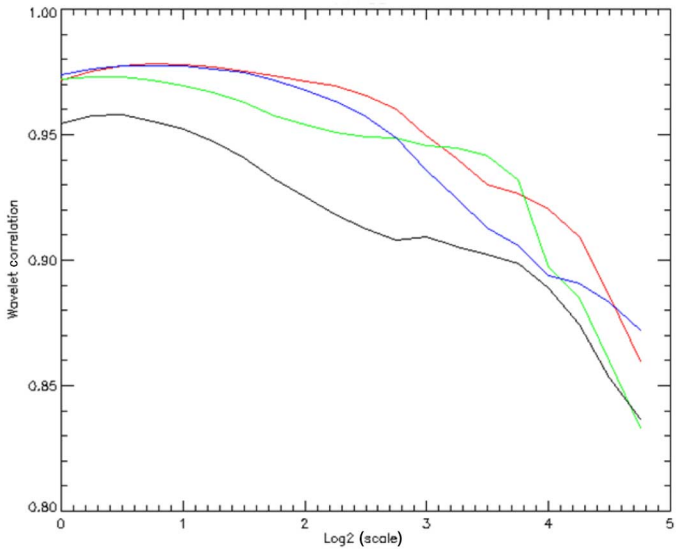

Fig. 6. Wavelet correlation between ENVISAT ASAR datasets acquired in 2006 and 2010 for four classes: DF (red), FS (green), IF (blue), and FAM (black).

indicate a nonstationary situation (increasing signature at all scale) corresponding to the presence of an edge.

E. Wavelet Covariance

The normalized wavelet covariance (correlation) signature (9) provides a measure of how the SAR backscatter within the estimation window (related to a specific landcover class) changes texturally between two dates and as a function of scale. It is therefore a spatiotemporal fingerprint of the SAR statistics. An example is shown in Fig. 6. The signature was computed with the same classes as the wavelet variance signature in Fig. 3 and refers to changes between acquisitions in 2006 and 2010. It can be observed that the wavelet variance of all classes loses correlation between the two dates, with lower correlation at longer scales. The changes at short scales may be influenced by residual speckle noise, whereas as scale increases, variation of the RCS spatial distribution comes into play. Class FAM (black) shows the highest decorrelation (highest temporal change) at all scales. This pattern depends obviously by temporal changes in the agricultural practices and bare soil extent. At short scales (up to 2^3), the statistics of class FS (green) shows more decorrelation than the ones of class intact and DF. Again, this is the other class where changes in the target can be expected. For class IF (blue), there appears to be more textural change in comparison with class DF. This feature must be further investigated to be able to connect it to vegetation changes.

VI. ALOS PALSAR Results and Interpretation

A. Wavelet Variance Signatures

The wavelet statistics analysis was also applied to L-band ALOS PALSAR at HH and HV polarizations. The signatures for the classes FS, IF, DF, and FAM can be found in Fig. 7(a) and (b). Differences of the wavelet statistics at HH and HV

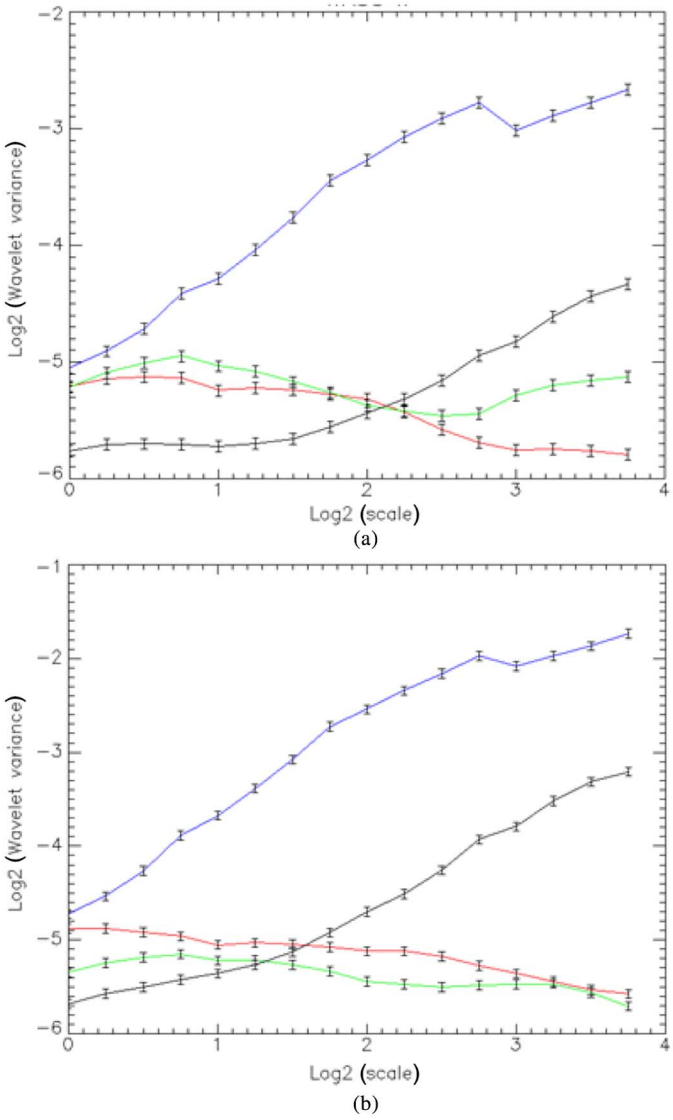

Fig. 7. (a) ALOS PALSAR HH and (b) ALOS PALSAR HV wavelet variance scaling signatures (four dyadic scales) for four classes of interest: FAM (blue), DF (red), IF (green), and FS (black) with corresponding error bars (black).

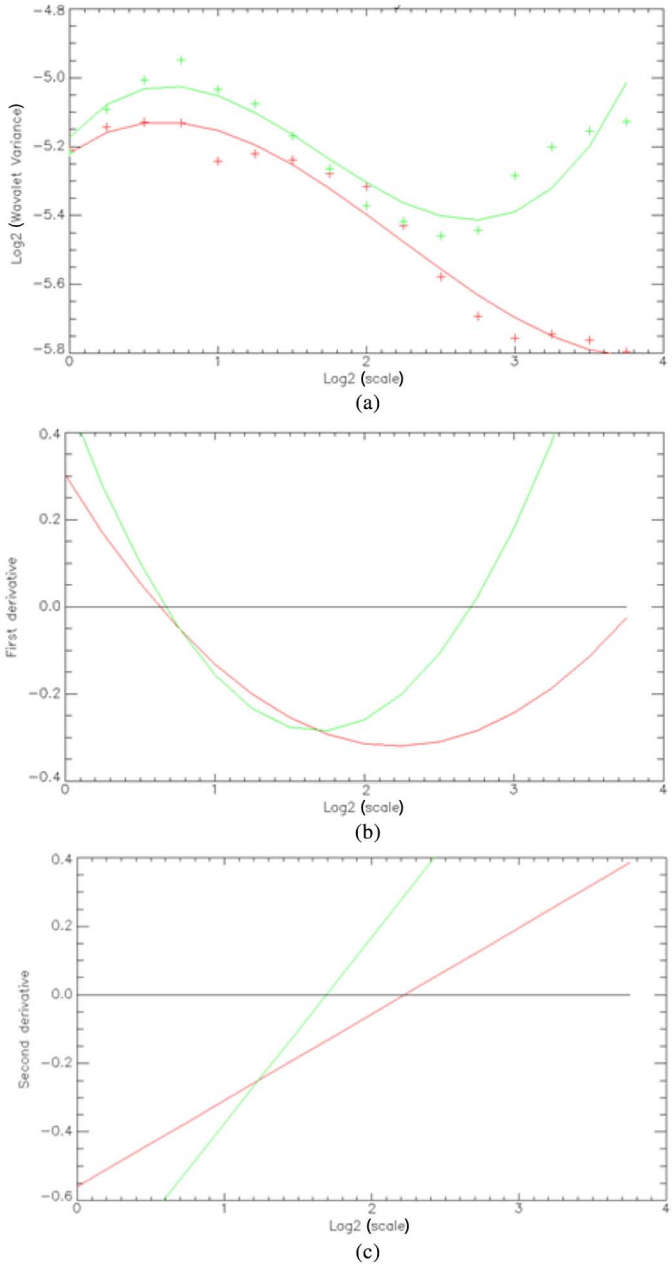

Fig. 8. (a) Wavelet scaling signature for two classes: IF (green cross) and DF (red cross) and the fitted third-degree polynomial functions (green and red solid lines). (b) First derivative of the fitted polynomial. (c) Second derivative of the fitted polynomial.

polarizations (in terms of absolute wavelet variance values and functional form) can be readily seen from the graphs.

At HH polarization, the scaling functional form of the signatures is similar to the one of ENVISAT ASAR VV, with the DF signature flattening out and the IF signature keeping memory of its structure [these trends are better highlighted with the fitted wavelet signatures in Fig. 8(a)]. While, at HV polarization, the signatures for the two classes reveal the onset of a white noise random process (no texture) and no significant difference between the two. We conclude that the HV return (volume scattering) does not provide spatial information that is useful to discriminate between DF and IF. From another standpoint, differences in biomass within and between intact and DF (if any) cannot be detected at this radiometric and spatial resolution by HV backscatter. On the other hand, the HH return is sensitive to the large scattering elements in the top layer of the canopy, and therefore, develops sensitivity to the forest structure in the same way as the C-band VV, although with less strength due to the increased penetration. The signatures of the two heterogeneous classes (FAM and FS), both at HH and HV, bear in a very strong way the tell-tale signs of nonstationarity, and even more so with respect to the ENVISAT ASAR case.

B. Wavelet Scaling Signatures Functional Analysis

This analysis is carried out only for HH polarization in view of IF and DF class separation, since the HV does not provide useful spatial information. The fitted wavelet signatures also confirm that the PALSAR HH is similar to the ASAR VV case in terms of functional form. However, the parameters that characterize univocally this dependence are different. Now,

the two classes present the same correlation length [Fig. 8(a)]. Therefore, the first zero crossing of the first derivative cannot be used as a marker [Fig. 8(b)]. On the other hand, now the second zero crossing is a good candidate, since it occurs at short scales for the IF, and at longer scales (if any) for the DF [Fig. 8(c)].

The inflection point (zero of the second derivative) appears to have the same role as in the case of ASAR. The significance of these observations was checked using a hypothesis test at 0.05 significance level of the differences of the mean values of these parameters (second zero crossing of the first derivative and zero crossing of the second derivative) using 20 samples for each class of interest.

The test reports that the H0 cannot be rejected in this case ($p = 0.109$). Therefore, functional analysis of wavelet signatures does not appear to be a viable solution for the textural discrimination of the two classes using ALOS PALSAR HH.

VII. Conclusion

Supervised analysis of SAR backscatter spatial statistics, as provided by a wavelet frame representation, was undertaken with the goal of assessing the capability of retrieving information about landcover differentiation, in particular, the ability to differentiate intact and DF in a closed semideciduous forest context. Test cases were developed using both C-band ENVISAT ASAR and L-band ALOS PALSAR datasets acquired on a site in Cameroon.

Results have shown that wavelet variance scaling signatures, which are measures of the SAR backscatter two-point statistics in the combined space-scale domain, are able to differentiate landcover classes by capturing their spatial distribution. This sensitivity extends the possibility of class discrimination based on intensity values distance, which is effective only for radiometrically pure classes or homogeneous targets, to the case of heterogeneous targets, these giving rise to texturally pure classes. Along this line, wavelet spectra were proven to be effective in characterizing heterogeneous landcover, such as FAM, by capturing the onset and the spatial location of singularities, such as edges.

Importantly, discrimination between IF and DF which is an important focus for conservation science was found to be enabled by functional analysis of the wavelet scaling signatures of C-band ENVISAT ASAR data. Analytic parameters, describing the functional form of the scaling signatures when fitted by a third-degree polynomial, resulted in a statistically significant difference between the signatures of the two classes. On the other hand, this outcome could not be replicated using the L-band ALOS PALSAR data.

Reasons for the inability to discriminate between intact and DF using ALOS PALSAR could be explained by the fact that L-band penetrates more into the canopy, and therefore, the observed backscatter texture is influenced more by the distribution of large scattering elements, and by the ground return. By contrast, C-band ENVISAT ASAR penetration is lower, and thus, the backscatter return comes primarily from the top of the canopy components, which produce a microtopography effect on the radar return due to their irregular vertical and horizontal distribution (e.g., emergent trees, which may be missing in degraded/regenerating forests). Additionally, differences in incidence angle and environmental/seasonal conditions between the C-band and L-band acquisitions could have influenced the differences in observed results.

The study area is characterized by DF that was disturbed by selective logging at least 15 years in the past. It is therefore notable that a SAR sensor at 15-m resolution can still distinguish between this DF stage and IF, based on textural features. Additional information could be retrieved from higher resolution sensors (e.g., Sentinel-1 or TanDEM-X).

In this specific environmental setting, the ENVISAT ASAR VV outperforms the ALOS PALSAR at HH and HV polarizations in terms of distinguishing between intact and DF. However, in a different environmental setting with other degradation patterns (e.g., more recent forest degradation patterns or in closed evergreen forest), the results could be different and therefore, testing the method in several areas will be undertaken in the future.

The performance of C-band ENVISAT ASAR for the purpose of discriminating between intact and DF is a promising result given the future availability of new C-band data provided by ESA Sentinel-1 mission.

Acknowledgment

The authors would like to acknowledge the software providers Sarmap SA (Sarscape 5.0) and the data providers: ESA (ENVISAT ASAR), Sarmap SA, JAXA (ALOS PALSAR), BlackBridge (RapidEye), and USGS (Landsat data).

References

[1] J. Grace, E. Mitchard, and E. Gloor, "Perturbations in the carbon budget in the tropics," *Global Change Biol*., vol. 20, pp. 3238–3255, Feb. 2014.

[2] O. Mertz *et al*., "The forgotten D: Challenges of addressing forest degradation in complex mosaic landscapes under REDD+," *Danish J. Geogr*., vol. 112, no. 1, pp. 63–76, May 2012.

[3] I. D. Thompson *et al*., "An operational framework for defining and monitoring forest degradation," *Ecol. Soc*., vol. 18, no. 2, p. 20, Jun. 2013.

[4] C. J. Oliver, "The interpretation and simulation of clutter textures in coherent images," *Inverse Prob*., vol. 2, pp. 481–518, Nov. 1986.

[5] Global Forest Observations Initiative. (2014, Jan.). *Integrating Remote-Sensing and Ground-Based Observations for Estimation of Emissions and Removals of Greenhouse Gases in Forests: Methods and Guidance from the Global Forest Observations Initiative* [Online]. Available: https://unfccc.int/files/methods/redd/submissions/application/pdf/redd_20140218_mgd_report_gfoi.pdf

[6] A. Ahrends *et al*., "Predictable waves of sequential forest degradation and biodiversity loss spreading from an African city," *Proc. Natl. Acad. Sci. USA*, vol. 107, no. 33, pp. 1–6, Aug. 2010.

[7] M. S. Mon, N. Mizoue, N. Z. Htun, T. Kajisa, and S. Yoshida, "Factors affecting deforestation and forest degradation in selectively logged production forest: A case study in Myanmar," *Forest Ecol. Manage*., vol. 267 no. 1, pp. 190–198, Mar. 2012.

[8] T. A. Stone and P. Lefebvre, "Using multi-temporal satellite data to evaluate selective logging in Para, Brazil," *Int. J. Remote Sens*., vol. 19, no. 13, pp. 2517–2526, Jan. 1998.

[9] M. Hirschmugl, M. Steinneger, H. Gallaun, and M. Schardt, "Mapping forest degradation due to selective logging by means of time series analysis: Case studies in Central Africa," *Remote Sens*., vol. 6, no. 1, pp. 756–775, Jan. 2014.

[10] C. M. Souza, Jr., D. A. Roberts, and M. A. Cochrane, "Combining spectral and spatial information to map canopy damage from selective logging and forest fires," *Remote Sens. Environ*., vol. 98, no. 2–3, pp. 329–343, Oct. 2005.

[11] C. M. Souza, Jr., and D. Roberts, "Mapping forest degradation in the Amazon region with Ikonos images," *Int. J Remote Sens.*, vol. 26, no. 3, pp. 425–429, Feb. 2005.

[12] J. Franke, P. Navratil, V. Keuck, K. Peterson, and F. Siegert, "Monitoring fire and selective logging activities in tropical peat swamp forests," *IEEE J. Sel. Topics Appl. Earth Observ. Remote Sens.*, vol. 5, no. 6, pp. 1811–1820, Dec. 2012.

[13] E. T. A. Mitchard *et al.*, "Mapping tropical forest biomass with radar and spaceborne LiDAR in Lopé National Park, Gabon: Overcoming problems of high biomass and persistent cloud," *Biogeosciences*, vol. 9, no. 1, pp. 179–191, Jul. 2012.

[14] S. Kuntz *et al.*, "A multi-stage inventory scheme for REDD inventories in tropical countries," in *Proc. 34th Int. Symp. Remote Sens. Environ.*, Sydney, Australia, Apr. 2011, pp. 1–4.

[15] J. Deutscher, R. Perko, K. Gutjahr, M. Hirschmugl, and M. Schardt, "Mapping tropical rainforest canopy disturbances in 3D by COSMO-skymed spotlight InSAR-stereo data to detect areas of forest degradation," *Remote Sens.*, vol. 5, no. 2, pp. 648–663, Feb. 2013.

[16] M. Schlund, F. von Poncet, D. Hoekman, S. Kuntz, and C. Schmullius, "Importance of bistatic SAR features from TanDEM-X for forest mapping," *Remote Sens. Environ.*, vol. 151, pp. 16–26, Aug. 2014.

[17] E. Attema *et al.*, "Sentinel-1. The radar mission for GMES operational land and sea services," *ESA Bull.*, vol. 131, pp. 1–17, Aug. 2007.

[18] H. Benelcadi *et al.*, "Contribution of TerraSAR-X radar images texture for forest monitoring," in *Proc. IEEE Int. Geosci. Remote Sens. Symp. (IGARSS)*, Jul. 2012, pp. 6427–6430.

[19] R. M. Haralick and W. F. Bryant, "Documentation of procedures for textural/spatial pattern recognition techniques," Univ. Kansas, Lawrence, KS, USA, Final Rep. 278-1, 1976, 203pp.

[20] L. R. Sarker, J. Nichol, H. B. Iz, B. B. Ahmad, and A. A. Rahman, "Forest biomass estimation using texture measurements of high-resolution dual-polarization C-band SAR data," *IEEE Trans. Geosci. Remote Sens.*, vol. 51, no. 6, pp. 3371–3384, Jul. 2013.

[21] M. Beauchemin, K. P. B. Thomson, and G. Edwards, "Edge detection and speckle adaptive filtering for SAR images based on a second-order textural measure," *Int. J. Remote Sens.*, vol. 17, no. 9, pp. 1751–1759, Jun. 1996.

[22] I. Daubechies, "Orthonormal bases of compactly supported wavelets," *Commun. Pure Appl. Math.*, vol. 41, no. 7, pp. 909–996, Oct. 1988.

[23] P. Kumar and E. Foufoula-Georgiou, "Wavelet analysis for geophysical applications," *Rev. Geophys.*, vol. 35, no. 4, pp. 385–412, Nov. 1997.

[24] M. E. J. Cutler, D. S. Boyd, G. M. Foody, and A. Vetrivel, "Estimating tropical forest biomass with a combination of SAR image texture and Landsat TM data: An assessment of predictions between regions," *ISPRS J. Photogramm. Remote Sens.*, vol. 70, pp. 66–77, Jun. 2012.

[25] M. Simard, G. De Grandi, K. P. B. Thomson, and G. B. Benie, "Analysis of speckle noise contribution on wavelet decomposition of SAR images," *IEEE Trans. Geosci. Remote Sens.*, vol. 36, no. 6, pp. 1953–1962, Nov. 1998.

[26] G. D. De Grandi, R. M. Lucas, and J. Kropacek, "Analysis by wavelet frames of spatial statistics in SAR data for characterizing structural properties of forests," *IEEE Trans. Geosci. Remote Sens.*, vol. 47, no. 2, pp. 494–507, Feb. 2009.

[27] M. Unser, "Texture classification and segmentation using wavelet frames," *IEEE Trans. Image Process.*, vol. 4, no. 11, pp. 1549–1560, Nov. 1995.

[28] V. Bellassen and V. Gitz, "Reducing emissions from deforestation and degradation in Cameroon—Assessing costs and benefits," *Ecol. Econ.*, vol. 68, no. 1–2, pp. 336–344, Dec. 2008.

[29] B. Martens, N. S. Gideon, S. Matthew, and T. Bertrand. (2012). *Interactive Forestry Atlas of Cameroon. Version 3.0* [Online]. Available: http://data.wri.org/forest_atlas/cmr/report/cmr_atlas_v3_eng.pdf

[30] B. Martens and E. F. Lambin, "Land-cover-change trajectories in Southern Cameroon," *Ann. Assoc. Amer. Geogr.*, vol. 90, no. 3, pp. 467–494, Sep. 2000.

[31] FAO. (1985). *Forest Genetic Resources. Information -No.14. In Situ Conservation of Forest Genetic Resources in Cameroon* [Online]. Available: http://www.fao.org/docrep/006/r4968e/r4968e07.htm

[32] Y. Yako Tegechouang. (2010). *Contribution a la gestion des relations homme-plantation forestiere dans le sud et l'Est Cameroun: Cas des plantations de Pericopsis elata de bidou ii dans la reserve de la kienke sud et du bloc kebe dans la reserve de Deng-Deng* [Online]. Available: http://www.itto.int/files/user/cites/cameroon/M%C3%A9moire_gestion%20des%20relations%20homme_Plantations_Yako%2024_05_2010.pdf

[33] World Bank. (2014). *Climate Change Knowledge Portal* [Online]. Available: http://sdwebx.worldbank.org/climateportal/index.cfm?page=country_historical_climate&ThisRegion=Africa&ThisCCode=CMR

[34] Sarmap. (2007). *SARscape Technical Description* [Online]. Available: https://www.exelisvis.com/portals/0/pdfs/ENVI/SAR_tech_documents/SARscape_Technical_Description.pdf

[35] G. F. De Grandi, M. Leysen, J. S. Lee, and D. Schuler, "Radar reflectivity estimation using multiple SAR scenes of the same target: Technique and applications," in *Proc. IEEE Int. Remote Sens. Sci. Vis. Sustain. Develop. Geosci. Remote Sens. (IGARSS'97)*, Aug. 3–8, 1997, vol. 2, pp. 1047–1050.

[36] World Resources Institute. (2014). *Congo Basin Forest Atlases* [Online]. Available: http://www.wri.org/our-work/project/congo-basin-forests/congo#project-tabs

[37] I. Daubechies, *Ten Lectures on Wavelets*. Philadelphia, PA, USA: Society for Industrial and Applied Mathematics, 1992, ch. 3.

[38] S. Mallat, *A Wavelet Tour of Signal Processing*. New York, NY, USA: Academic, 1998, ch. 5.5, pp. 148–156.

[39] M. J. Shensa, "The discrete wavelet transform: Wedding the à trous and Mallat algorithms," *IEEE Trans. Signal Process.*, vol. 40, no. 10, pp. 2464–2482, Oct. 1992.

[40] S. Mallat, *A Wavelet Tour of Signal Processing*. New York, NY, USA: Academic, 1998, ch. 6.3, pp. 198–199.

[41] G. De Grandi, J.-S. Lee, and D. L. Schuler, "Target detection and texture segmentation in polarimetric SAR images using a wavelet frame: Theoretical aspects," *IEEE Trans. Geosci. Remote Sens.*, vol. 45, no. 11, pp. 3437–3453, Nov. 2007.

[42] A. Davis, A. Marshak, and W. Wiscombe, "Wavelet-based multifractal analysis of non-stationary and/or intermittent geophysical signals," in *Wavelets in Geophysics*, E. Foufoula-Georghiou and P. Kumar, Eds. New York, NY, USA: Academic, 1994, pp. 249–298.

[43] F. T. Ulaby, F. Kouyate, B. Brisco, and T. H. Williams, "Textural information in SAR images," *IEEE Trans. Geosci. Remote Sens.*, vol. 24, no. 2, pp. 235–245, Mar. 1986.

[44] C. J. Oliver, "A model for non-Rayleigh scattering statistics," *Opt. Acta Int. J. Opt.*, vol. 31, no. 6, pp. 701–722, 1984.

[45] C. J. Oliver, "The representation of correlated clutter textures in coherent images," *Inverse Prob.*, vol. 4, pp. 843–866, 1988.

[46] D. R. Sheen and L. P. Johnston, "Statistical and spatial properties of forest clutter measured with polarimetric synthetic aperture radar (SAR)," *IEEE Trans. Geosci. Remote Sens.*, vol. 30, no. 3, pp. 578–588, May 1992.

[47] L. Kurvonen and M. T. Hallikainen, "Textural information of multitemporal ERS-1 and JERS-1 SAR images with applications to land and forest type classification in boreal zone," *IEEE Trans. Geosci. Remote Sens.*, vol. 37, no. 2, pp. 680–689, Mar. 1999.

[48] M. J. Collins and J. Huang, "Uncertainties in the estimation of ACF-based texture in synthetic aperture radar image data," *IEEE Trans. Geosci. Remote Sens.*, vol. 36, no. 3, pp. 940–949, May 1998.

[49] F. Bujor, E. Trouve, L. Valet, J.-M. Nicolas, and J.-P. Rudant, "Application of log-cumulants to the detection of spatiotemporal discontinuities in multitemporal SAR images," *IEEE Trans. Geosci. Remote Sens.*, vol. 42, no. 10, pp. 2073–2084, Oct. 2004.

[50] D. B. Percival and A. T. Walden, *Wavelet Methods for Time Series Analysis*. Cambridge, U.K.: Cambridge Univ. Press, 2000, ch. 8.3, p. 306.

[51] B. Picinbono, *Random Signals and Systems*. Englewood Cliffs, NJ, USA: Prentice Hall, 1993, ch. 5.4.

[52] C. V. Stewart, B. Moghaddam, K. J. Hintz, and L. M. Novak, "Fractional Brownian motion models for SAR imagery scene segmentation," *Proc. IEEE*, vol. 81, no. 10, pp. 1511–1522, Oct. 1993.

[53] G. Franceschetti, A. Iodice, M. Migliaccio, and D. Riccio "Scattering from natural rough surfaces modeled by fractional Brownian motion two-dimensional processes," *IEEE Trans. Antennas Propag.*, vol. 47, no. 9, pp. 1405–1415, Sep. 1999.

[54] G. W. Wornell, "Wavelet-based representations for the 1/f family of fractal processes," *Proc. IEEE*, vol. 81, no. 10, pp. 1428–1450, Oct. 1993.

Elsa C. De Grandi (M'09) received the B.Sc. degree in physical geography and the M.Sc. degree (with distinction) in remote sensing and geography from Aberystwyth University, Aberystwyth, U.K., in 2011 and 2012, respectively. Currently, she is pursuing the Ph.D. degree in remote sensing of forests at the University of Edinburgh, Edinburgh, U.K.

She is a Co-Investigator of the German Aerospace Center (DLR) TanDEM-X science program. Her research interests include the use of synthetic aperture radar (SAR) to map forest changes and forest degradation in tropical forest.

Edward Mitchard (M'07) was born in U.K., in 1986. He received the Degree in biological sciences from the University of Oxford, Oxford, U.K., in 2007, and the Ph.D. degree in remote sensing of forests from the University of Edinburgh, Edinburgh, U.K., in 2011.

Currently, he is a Chancellor's Fellow with the University of Edinburgh, and previously held a NERC Fellowship there. He has authored extensively, including in *PNAS*, *Geophysical Research Letters*, and *Nature Climate Change*. His research interests include the use of remote sensing data (optical, radar, and lidar) to map aboveground biomass and vegetation type, and changes in these parameters.

Dr. Mitchard is also a Member of the European Geosciences Union and chairs the Technical Advisory Board of the Plan Vivo Foundation.

Iain H. Woodhouse received the B.Sc. degree (Hons.) from the University of Edinburgh, Edinburgh, U.K., the M.Sc. degree in remote sensing from Dundee University, Dundee, U.K., and the Ph.D. degree in atmospheric remote sensing from the Heriot-Watt University, Edinburgh.

He has worked with the Marconi Research Center and Wageningen University, Wageningen, The Netherlands. In 1999, he moved to the University of Edinburgh, where he is currently a Senior Lecturer in Radar Remote Sensing with the School of GeoSciences. He is a Principal Investigator on a number of projects related to quantitative measurements of forests from remote sensing, which are funded by NERC, DTI, DSTL, and the Forestry Commission. His research interests include retrieval of biophysical properties of vegetation using active remote sensing, specifically synthetic aperture radar (SAR), and lidar.

Dr. Woodhouse is a Member of the NERC Earth Observation Director's Advisory Board and the Group on Earth Observations (GEO) Capacity Building Committee and a Nonexecutive Director of Ecometrica Ltd. He was a Founding Member of the Edinburgh Earth Observatory (EEO), a research group within the School of GeoSciences.

Gianfranco D. De Grandi (M'90–SM'96–F'02) received a Doctorate degree (Hons.) in physics engineering from Politecnico Milano, Milan, Italy, in 1973.

From 1977 to 2012, he was with the European Commission Directorate General Joint Research Center, Ispra, Italy, where he performed research in signal processing for application areas such as gamma ray spectroscopy, data communications, and radar remote sensing. In 1985, he was a Visiting Scientist at Bell Communications Research, Morristown, NJ, USA, where he participated in the design of metrocore, one of the first research projects for Gbit rate metropolitan area networks. From 1997 to 2001, he served as an Assistant Professor with the Faculte' de Foresterie et Geomatique, Universite' Laval, Quebec, PQ, Canada. He was a Principal Investigator of Japan Aerospace Exploration Agency (JAXA) Global Boreal Forest Mapping project, the ALOS research program, and the Kyoto and Carbon (K&C) project. He is an Investigator of the German Aerospace Center (DLR) Tandem-X science program. Currently, he is a Visiting Scholar at the Aberystwyth University, Aberystwyth, U.K., where he is pursuing his research interests in SAR spatial statistics.